Nanoscale

Accepted Manuscript

This article can be cited before page numbers have been issued, to do this please use: G. Manoharan, X. Li, S. Dimitrov and M. Palma, *Nanoscale*, 2026, DOI: 10.1039/D6NR00390G.

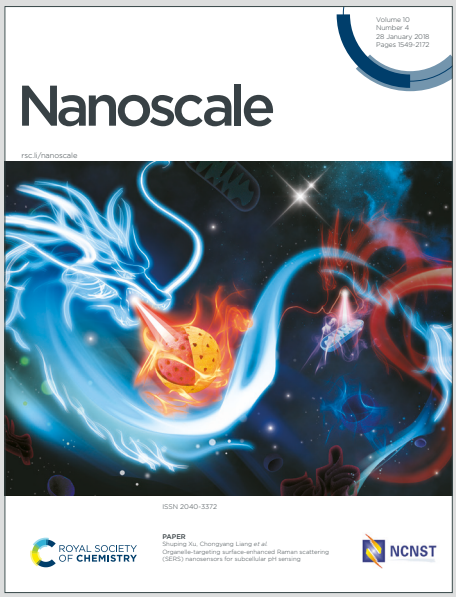

ROYAL SOCIETY OF CHEMISTRY

rsc.li/nanoscale

View Article Online
DOI: 10.1039/D6NR00390G

ARTICLE

Templated Growth of Perovskite Shells on Single Walled Carbon Nanotubes: A Solution Processable Route Towards Tailored Devices

Received 00th January 20xx,
Accepted 00th January 20xx

DOI: 10.1039/x0xx00000x

Gririraj Manoharan, Xuan Li, Stoichko Dimitrov* and Matteo Palma*

Carbon nanotubes (CNTs) based nanohybrids have shown considerable potential for the construction of functional heterostructures with a diverse range of optoelectronic properties. To fully exploit their potential, high-performance solution-processed semiconductors with precisely controlled optical and electronic characteristics are desirable. In this regard, halide perovskite semiconductors are known for their excellent and tunable optoelectronic properties and hence are an ideal candidate to be integrated into CNT-based nanohybrids towards the construction of systems and devices with enhanced functionality. Here we present a strategy for the synthesis of solution-processable nanohybrids made of single-walled carbon nanotubes (SWCNTs) and perovskites semiconductors, using methylammonium-lead-iodide ($MAPbI_3$) and Cesium Lead Iodide ($CsPbI_3$) as proof-of-concept systems: the CNTs act as templates for the facile and tunable formation of perovskite nanocrystals. We investigated the structural and electronic properties of the assembled SWCNT-heterostructures and demonstrated their integration (from solution) in field-effect transistor device configurations. By harnessing the synergistic properties of carbon nanotubes and perovskites, we discuss pathways for the development of photoresponsive devices employing these nanohybrids. The facile, solution-processable methodology we developed enables the spatial positioning of SWCNT-perovskite intermediate nanohybrids prior to crystallization, allowing the integration of nanoscale SWCNT bundles into FET architectures toward optoelectronic applications.

Introduction

The ability to combine the structural and optoelectronic properties of different nanomaterials into novel heterostructures with enhanced functionality is of great interest, in particular for optoelectronic applications[1-3]. In this context, carbon nanotubes (CNT) based nanohybrids have drawn attention due to the one-dimensional (1D) charge transport character of the nanotubes, their high surface area, and the resulting ability to facilitate charge transfer at heterointerfaces for the generation of low-dimensional heterostructures with tunable electronic, optical, and mechanical properties[1, 3-9]. Of particular interest is the integration of CNTs with materials that possess tunable optical and electronic properties[1-3, 10, 11]. Among these, perovskite semiconductors have shown great potential since the first reports of high-performance perovskite solar cells in 2012[12-15]. They have the general formula ABX_3 (where A = $CH_3NH_3^+$ [methylammonium (MA)], $CH(NH_2)_2^+$ [formamidinium (FA)], Cs^+; B = Pb^{2+}, Sn^{2+}; and X = I^-, Br^-, Cl^-) and have found different optoelectronics applications, from use in field-effect transistors,[16, 17] to light-emitting diodes (LEDs)[18, 19] photodetectors,[20, 21] solar cells[22] and gas sensors[23]. Advantages of perovskites are their solution processability and lightweight nature, which can simplify device fabrication without sacrificing performance. Furthermore, perovskite semiconductors are multi-crystalline and exhibit high light absorption coefficients, tunable band gaps, high photoluminescence quantum yields, and long carrier diffusion lengths, making them highly attractive for integration into hybrid nanostructures[24-27].

In this regard, the integration of multi-walled (MW) and single-walled (SW) CNTs with perovskites has been investigated primarily as thin films or dopants, demonstrating the potential of these heterostructures for optoelectronic applications[22, 28-36]. The synergy between perovskite and carbon nanotubes has recently paved the way for highly sensitive, flexible and stable next generation neuromorphic sensor arrays and advanced photodetectors[37-42]. For instance, SWCNTs were spray coated as aligned arrays, followed by the spin coating of metal halide perovskite thin films onto pre-patterned substrates, to facilitate the demonstration of optical switching behavior[43]. More recently, Wang et al. reported a growth strategy on SWCNT thin films, achieving high performance through optimized interface engineering with ligand coated perovskite quantum dots[29]. Growing perovskite nanocrystals inside the CNTs has also been established via melt insertion, gas/liquid phase infiltration

[a] Department of Chemistry, Queen Mary University of London, London E1 4NS, United Kingdom.
† Footnotes relating to the title and/or authors should appear here.
Supplementary Information available: [details of any supplementary information available should be included here]. See DOI: 10.1039/x0xx00000x

View Article Online
DOI: 10.1039/D6NR00390G

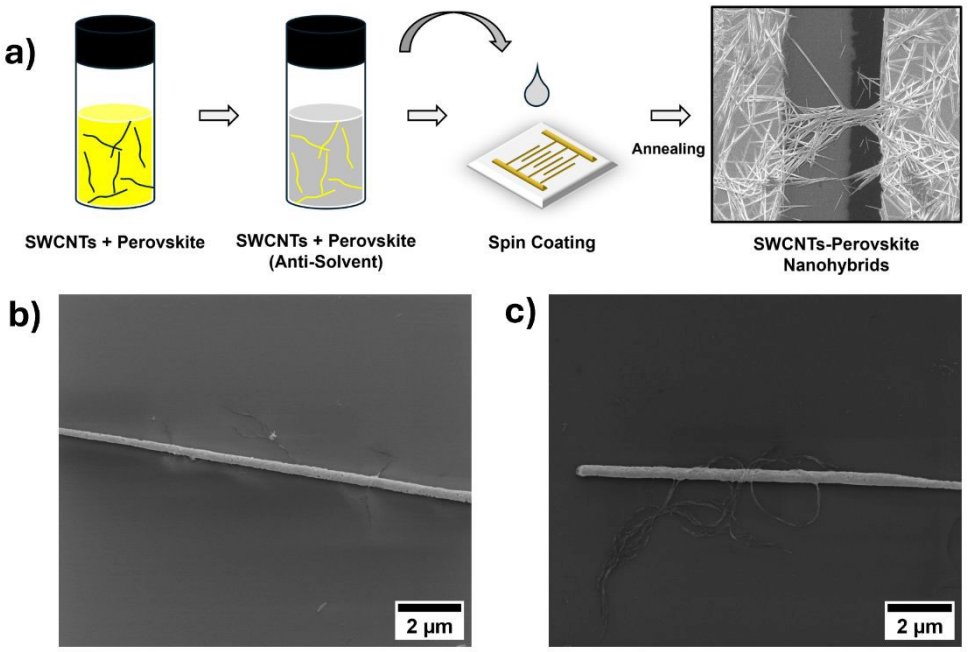

Figure 1. a) Schematic of the step-by-step procedure of perovskite nanocrystals ($MAPbI_3$ and $CsPbI_3$) growth on single walled carbon nanotubes and representative SEM image of the device. SEM images of resulting nanohybrids: b) (7,6) SWCNT-$MAPbI_3$ and c) (6,5) SWCNT-$MAPbI_3$.

yielding an atomically resolved interface structure for ultra-low power transistors and X-ray detectors[44-47]. However, only a limited number of studies have demonstrated growing perovskite nanocrystals directly on the surface of the CNTs, and have done this employing MWCNTs[4, 28, 48] which have limited utility as transistor channels[49]. Notably, Lee et al. demonstrated a nano seeding strategy to grow perovskite nanocrystals on MWCNTs, subsequently employed as green-emitting nanohybrids for UV detection and anticounterfeiting QR codes[28].

In this study, we developed a strategy to grow perovskite nanocrystals as shells on SWCNTs, and fabricated photoresponsive devices comprising CNT-perovskite nanohybrids. This strategy offers unique flexibility enabling growth of nanohybrids under annealing conditions and can be potentially tailored to specific device configurations. We demonstrated the general applicability of our strategy employing semiconducting SWCNTs of two distinct chirality, namely (7,6) and (6,5), and with two different perovskite materials, namely methylammonium-lead-iodide ($MAPbI_3$) and cesium lead iodide ($CsPbI_3$). The coupling between the two nanomaterials in the hybrid was investigated via structural and spectroscopic characterizations. As proof-of-concept, solution-processable photo responsive devices with high responsivity and detectivity were fabricated and characterized. Our method for synthesizing SWCNT-perovskite nanohybrids enables the construction of nanomaterials with direct and continuous hetero-interfaces, for potential applications in optoelectronics, sensing and communication[4, 50-52].

Results and Discussion

Hybrid SWCNT-perovskite structures were prepared from solution for four hybrid combinations, using SWCNTs with (7,6) and (6,5) enriched chirality (see Figure S1) as templates to grow two types of perovskites: Methylammonium Lead Iodide ($MAPbI_3$) and Cesium Lead Iodide ($CsPbI_3$). A three-step perovskite crystallisation approach was developed for their synthesis [details of the methodology are presented in the Experimental Section]. In the first step, perovskite precursors were mixed with the SWCNTs in dimethyl formaldehyde (DMF). Ethyl acetate (EA) antisolvent was then introduced to the solution to facilitate perovskite nucleation[48, 53]. In the third step, the solutions were deposited on surfaces and annealed to induce perovskites crystal growth on the SWCNTs nanotube bundles. The step-by-step synthetic approach including the representative scanning electron microscopy SEM image of a SWCNT-perovskite nanohybrid device is shown in Figure 1a. The morphology and uniformity of the SWCNT-perovskite nanohybrid were first examined using transmission and scanning electron microscopy (TEM and SEM); the results are shown in Figures 1b and c and Figure S2 a-f.

SEM and TEM imaging revealed nanocrystals on the surfaces of the SWCNTs, with growth occurring selectively on the nanotube surfaces and independently of SWCNT chirality. The average height distribution of the nanohybrids was found to be 26.3 nm with a standard deviation (SD) of 8.6 nm, highlighting the formation of bundles of SWCNT-perovskite nanohybrids (see Figure S3 AFM images of a typical SWCNT-perovskite

View Article Online
DOI: 10.1039/D6NR00390G

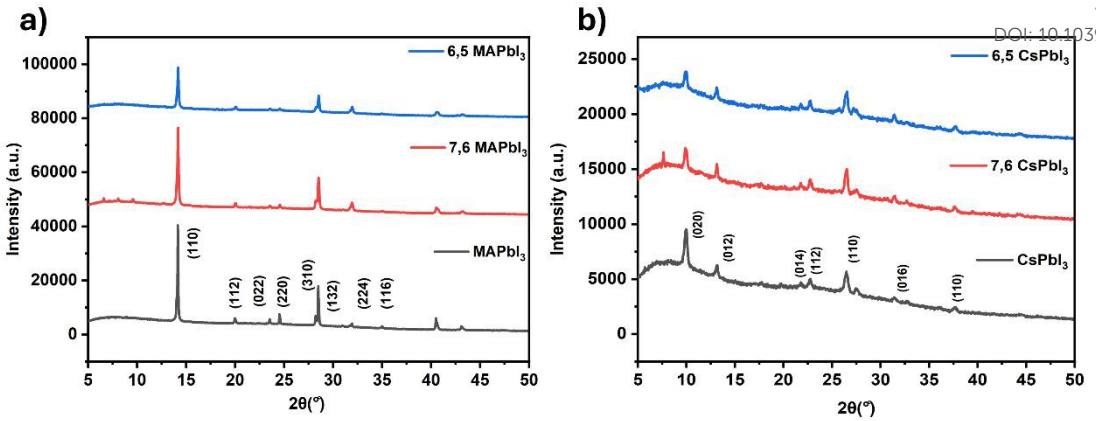

Figure 2. XRD patterns of (7,6) and (6,5) SWCNT-Perovskite Nanohybrids: a) SWCNT-$MAPbI_3$ b) SWCNT-$CsPbI_3$, with neat $MAPbI_3$ and $CsPbI_3$ films respectively.

nanohybrid bundle and its corresponding height profile). SEM images further confirmed the specificity of the growth, demonstrating dense crystal formation without significant pinholes, as highlighted in the Figures 1b and 1c [see Figure S2 a-f TEM images of perovskite nanohybrid bundles with (7,6), (6,5) and mixed chirality short (ss) SWCNTs, and Figure S4 HRTEM images with corresponding EDS mapping and spectra].

Figure 2 presents the X-ray diffraction (XRD) patterns of the nanohybrids containing (7,6) and (6,5) nanotubes, compared to $MAPbI_3$ and $CsPbI_3$ films. This analysis substantiates the growth of $MAPbI_3$ nanocrystals (Figure 2 a) on the SWCNTs, with distinctive peaks observed at 14.1°, 28.5°, 32.0°, and 40.6°, corresponding to the (110), (220), (310), and (224) planes of the orthorhombic perovskite crystal structure[54]. Figure 2b shows the characteristic diffraction peaks of $CsPbI_3$ nanocrystals grown on (7,6) and (6,5) at 10°, 13.11°, 22.6°, 26.47°, 31.39° and 37.66°, assigned to (020), (012), (112), (110), (016), and (110) planes of orthorhombic γ-phase[55-57]. The comparatively lower intensity of these peaks for SWCNT-perovskite hybrids, relative to pure perovskite thin films, can be due to formation of bundles on the substrate surface making it less dense. X-ray photoelectron spectroscopy (XPS) analysis of Pb 4f and I 3d for both $MAPbI_3$ and $CsPbI_3$ (Figures S5 and S6) , revealed a small shift in the binding energy likely related to electronic interactions between SWCNT and $MAPbI_3$ perovskite crystals, as previously shown in similar systems[4].

Raman spectroscopy investigations provided insight into the electronic interactions between the perovskites and the (7,6) and (6,5) SWCNTs. In the pristine SWCNTs, the G and G' bands were located at 1594 cm^{-1} and 2602.7 cm^{-1} for the (7,6) chirality, and 1590 cm^{-1} and 2592.5 cm^{-1} for the (6,5) chirality, consistent with literature values[58]. A blue shift in the G' band was identified for all SWCNT-perovskite nanohybrids, with peak values recorded at 2701.2 cm^{-1} for (7,6) $MAPbI_3$, 2710.99 cm^{-1} for (7,6) $CsPbI_3$, 2690.5 cm^{-1} for (6,5) $MAPbI_3$, and 2692.14 cm^{-1} for (6,5) $CsPbI_3$ respectively. This shift has been previously assigned to a decreased electron density in the SWCNT π-network, suggesting a net hole transfer from the perovskite nanocrystals to the SWCNTs; lattice-induced strain from the perovskite shell growth might also contribute to the observed shifts. [32, 43, 59-61].

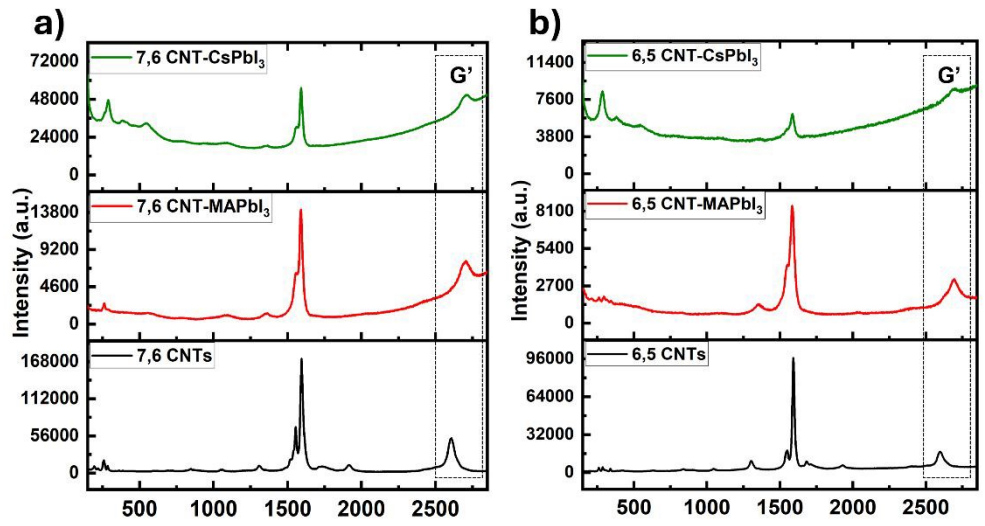

Figure 3. Raman spectra of (a) 7,6 SWCNT-based and b) 6,5 SWCNT-based pristine nanotubes and nanotube-perovskite nanohybrids ($MAPbI_3$ and $CsPbI_3$).

View Article Online
DOI: 10.1039/D6NR00390G

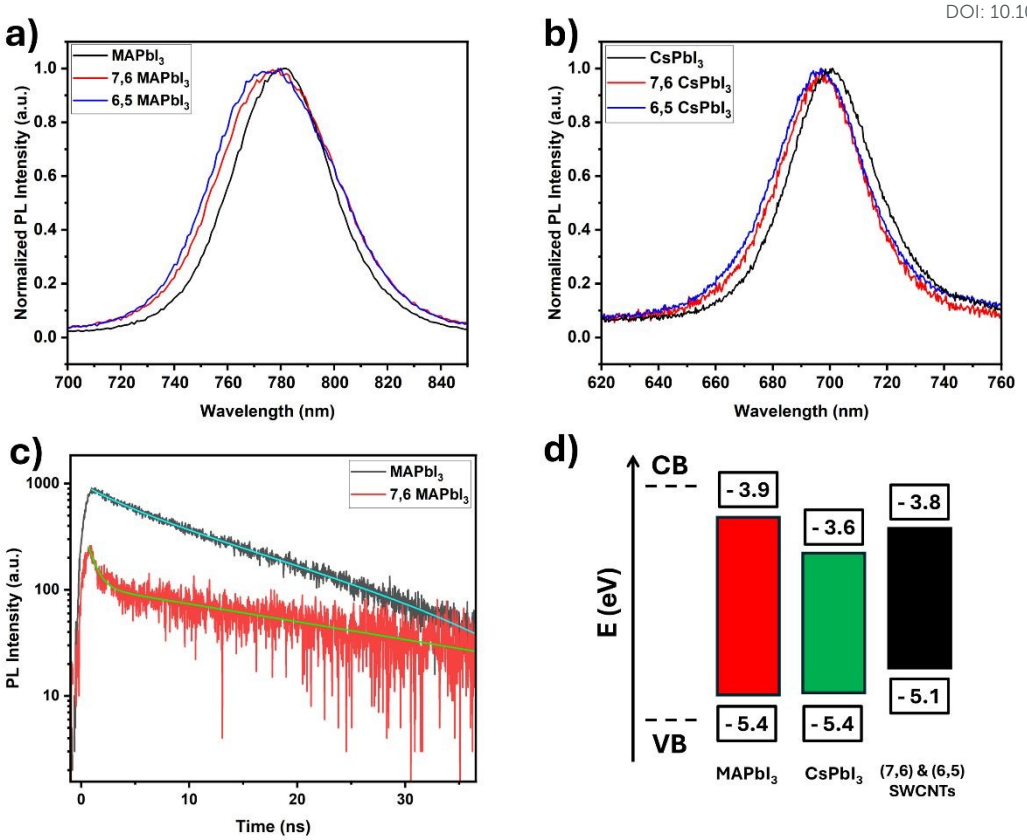

Figure 4. Steady-state photoluminescence spectra of perovskite films (a) $MAPbI_3$ and (b) $CsPbI_3$, and their perovskite nanohybrids with (7,6) and (6,5) SWCNT, acquired with 405 nm excitation. c) Time-resolved photoluminescence of $MAPbI_3$ and (7,6) SWCNT-$MAPbI_3$ nanohybrids using 635 nm laser illumination. d) Schematic illustration of the energy band diagram of $MAPbI_3$, $CsPbI_3$ and the (7,6) & (6,5) SWCNTs.

Photoluminescence (PL) spectroscopy characterization of our SWCNT-perovskite hybrids detected emission from the perovskite crystals. While neat perovskite films displayed PL peaks at 780 nm for $MAPbI_3$ and 700 nm for $CsPbI_3$, the CNT-perovskite nanohybrids exhibited a small blue shift for both types of perovskites in the nanohybrids (Figures 4a and 4b). This shift is potentially attributable to the Burstein-Moss effect[4], and consistent with the energy shifts in XPS and Raman caused by charge transfer from perovskite nanocrystals to carbon nanotubes. The broadening of the $MAPbI_3$ PL spectra in the two nanohybrids can be caused by variations in defect properties and interaction-induced strain, as the perovskite crystallites are grown on the SWCNT seed. The XRD results in Figure 2 do not show any changes in the bulk crystal lattice for this sample, suggesting that surface defects are responsible for the observed spectral changes. We further characterized mixed chirality (ss) SWCNT-perovskite nanohybrids, and they also exhibited the same PL characteristics (Figure S7). Moreover, we observed quenching of the PL emission of the nanotubes upon formation of perovskite nanohybrids (Figure S8), strongly indicating an electronic coupling between the CNTs and the perovskites.

The electronic coupling in the nanohybrids was further corroborated and quantified via time-resolved PL spectroscopy characterisations, employed to assess decay dynamics of the electronic excitations in the (7,6) SWCNT-$MAPbI_3$ (Figure 4c). The samples were excited with a 635 nm laser diode, and PL was detected at the perovskite emission maximum at 778 nm. The PL decay of $MAPbI_3$ was nearly mono-exponential, while the hybrids displayed a clear bi-exponential decay. The PL lifetime was found to decrease from 3.8 ns for $MAPbI_3$, to 0.7 ns in the SWCNT-$MAPbI_3$ nanohybrids. This indicates a strong quenching of photoexcited charges, most likely due to charge transfer between the SWCNT and the perovskite crystals. The electronic structure of the perovskites and the SWCNTs[62-65] suggests that the dominant charge transfer process can be ascribed to a hole transfer from the perovskite to the nanotubes (see Figure 4d), revealing close electronic coupling between the two nanostructures. The photoinduced charge transfer processes we observe in the SWCNT-perovskite nanohybrids make these heterostructures promising for optoelectronic applications[33, 35, 66].

nanotubes, in accordance with the PL data and band alignment

View Article Online
DOI: 10.1039/D6NR00390G

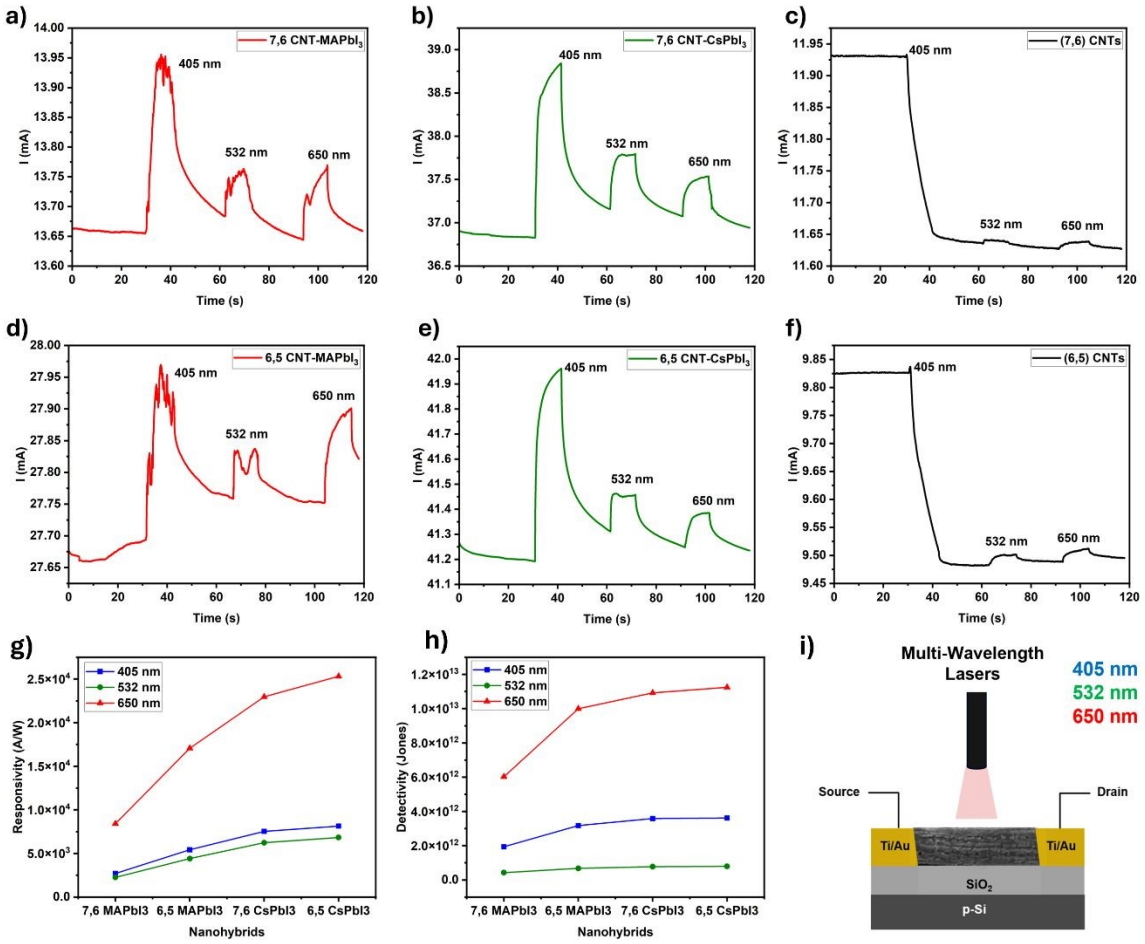

Figure 5. Photoresponse of SWCNT devices and SWCNT-Perovskite nanohybrids upon laser illumination with 405 nm, 532 nm and 650 nm wavelengths: a) (7,6) CNT-$MAPbI_3$, b) (7,6) CNT-$CsPbI_3$, c) pristine (7,6) SWCNTs, d) (6,5) CNT-$MAPbI_3$, e) (6,5) CNT-$CsPbI_3$, and f) Pristine (6,5) SWCNTs. g) Photoresponsivity (R) and h) Detectivity (D*) of the (7,6) and (6,5) carbon nanotube perovskite nanohybrids for three different wavelengths (405 nm, 532 nm and 650 nm, uncorrected for photon intensity), i) Cartoon of photoresponse characterization SWCNT-perovskite nanohybrids FET device.

In this regard, we fabricated phototransistor devices by spin-coating the SWCNT-perovskite intermediate nanohybrids solutions onto gold-plated interdigitated electrodes exhibiting a gap of 3 µm, patterned on Si/SiO_2 substrates (see the SI). Field-effect transistor (FET) devices exhibited a typical p-type behaviour, as expected for pristine semiconducting SWCNTs (Figure S9). Post annealing, the SWCNT-perovskite devices were illuminated for 10 s at 20 s intervals using consecutively laser diodes with the wavelengths: 650 nm, 532 nm, and 405 nm. Photocurrent was measured (in vacuum) through the source (S) and drain (D) electrodes with a constant S-D bias (V_{DS}) of 1 V. All the (7,6), (6,5) and (ss) SWCNT-perovskite nanohybrids exhibited a positive photocurrent change upon illumination at all three wavelengths (Figures 5a, 5b, 5c, 5d, S10a and S10b), while the pristine SWCNTs exhibited the aforementioned decrease at 405 nm, and minimal response at 532 nm and 650 nm illumination (Figures 5c, 5f and S7c). The behaviour in our SWCNT-perovskite nanohybrids is consistent with a photoinduced hole transfer from the perovskite nanocrystals to rationalisation discussed above (Figure 4). Stability tests performed on a SWCNT-$MAPbI_3$ photoresponsive device stored in air for one week showed consistent performance, while reproducibility tests on multiple devices fabricated from different batches exhibited similar photoresponse characteristics. (Figure S11 and S12). In order to quantify the photodetectors performance, we determined the photoresponsivity (R) and specific detectivity (D*) of all our SWCNT-perovskite devices at 405 nm, 532 nm and 650 nm light illuminations (Figures 5g and 5h and Tables S13 and S14). We observed the highest photoresponsivity and detectivity values at 650 nm illumination. In particular, the responsivity values at 650 nm for the SWCNT-$MAPbI_3$ nanohybrids were found to be 8.42×10^3 A/W and 1.71×10^4 A/W, for (7,6) and (6,5) $MAPbI_3$ respectively, while we measured responsivity values of 2.30×10^4 A/W, and 2.53×10^4 A/W for (7,6) and (6,5) $CsPbI_3$ nanohybrids, respectively. The highest detectivity (D*) was found to be 6.02×10^{12} Jones for (7,6) $MAPbI_3$ and 1×10^{13} Jones for (6,5) $MAPbI_3$ at 650 nm, while $CsPbI_3$ nanohybrids

View Article Online
DOI: 10.1039/D6NR00300E

detectivity was determined to be 1.09×10^{13} Jones for (7,6) $CsPbI_3$ and 1.12×10^{13} Jones for (6,5) $CsPbI_3$ at 650 nm.

Previous reports on CNT-perovskite photodetectors, primarily based on thin-film architectures, have demonstrated admirable performance at shorter wavelengths, with responsivities in the range of 1.6×10^6 A/W - 1.65×10^7 A/W and detectivities range reaching 3.1×10^{15} Jones - 2×10^{16} Jones at 405 nm, and up to 6.3×10^4 A/W and 1.12×10^{17} Jones at 532 nm[29, 37]. In comparison, our devices comprising limited individual SWCNT-perovskite nanohybrid bundles (~26.3 nm) exhibited responsivities of 3.74×10^3 - 7.02×10^3 A/W and detectivities of 1.44×10^{12} - 3.31×10^{12} Jones at 405 nm, and responsivities of 4.65×10^3 - 1.08×10^4 A/W with detectivities of 2.79×10^{12} - 5.90×10^{12} Jones at 532 nm. While these values are modest relative to the best-performing thin-film systems, they are among the highest reported for nanoscale, bundle-based SWCNT-perovskite architectures. Notably, at 650 nm where literature performance is limited[38], our devices achieved superior responsivities up to 2.53×10^4 A/W and detectivities up to 1.12×10^{13} Jones. These findings highlight the potential of our nanohybrid bundle design for efficient broadband photodetection, particularly in the red spectral region[29, 35, 37-42].

Conclusions

In summary we presented a facile solution processable strategy for the growth of perovskite nanocrystals as shells on SWCNTs. (7,6), (6,5) and mixed chirality short (ss) SWCNTs were employed as templates in the synthesis of two types of perovskites ($MAPbI_3$ and $CsPbI_3$), resulting in the formation of SWCNT-perovskite nanohybrids. XRD and PL spectroscopy characterizations confirmed the formation of perovskites, while SEM and TEM showed uniform and dense perovskite coverage of SWCNT bundles. Electronic interactions between the perovskites and SWCNTs were detected by XPS and Raman spectroscopy, while steady-state and time-resolved PL experiments allowed us to cast light on the photoinduced charge transfer processes among the hybrid components. Moreover, we fabricated solution-processable SWCNT-perovskite FET devices; these exhibited photocurrent responses consistent with a hole transfer process from the perovskite to the SWCNTs, corroborating the aforementioned PL spectroscopy investigations. Finally, high responsivity and detectivity values were determined in our nanohybrid devices, broadly in line with most of the previously presented perovskite-CNT thin films photodetectors. Notably, we achieved selective growth of perovskite nanocrystals on SWCNTs, and fabricated devices employing only a limited number of hybrids in bundles bridging prepatterned electrodes. Our approach for the direct growth of perovskites nanocrystals on SWCNTs is of general applicability, and the solution processable strategy allows spatial positioning of SWCNT-perovskite intermediate nanohybrids prior to crystallization, enabling tuning of the annealing and integration of nanoscale SWCNTs bundles in device configuration. This can pave the way to the development of future perovskite nanohybrid structures to be employed in various device architectures for diverse optoelectronic applications. SWCNTs have smaller sizes and, most importantly, chirality-dependent optoelectronic properties[67], making them compatible with the requirements of computing and electronic devices[68-70]. Integrating SWCNTs can offer various advantages for the formation of SWCNT-perovskite nanohybrids with enhanced functionality in optoelectronic applications[43, 71].

Experimental Section

1. Materials Preparation and Device Fabrication

1.1 Materials

Single-walled carbon nanotubes (SWCNTs) of chiralities including (7,6) (77% carbon nanotubes) and (6,5) (95% carbon nanotubes) were purchased from Sigma Aldrich. Short (ss) SWCNTs mixed chirality nanotubes (90% carbon nanotubes) were purchased from US Research Nanomaterials, Inc., N, N dimethylformamide (DMF, 99.8 % anhydrous), Ethyl Acetate (EA), Methyl Ammonium Iodide (CH_3NH_3I), Cesium Iodide (CsI) and Lead Iodide (PbI_2) were all used as purchased from Sigma Aldrich and used as received.

1.2 Dispersion of SWCNTs

0.5 mg of SWCNTs of chiralities including (7,6), (6,5), and short (ss) SWCNTs mixed chirality nanotubes were separately dispersed in 1 mL DMF through ultrasonication (Branson 2800, 130 W). The dispersion process of these three batches was carried out for 2 hours to ensure effective separation of nanotubes. Following ultrasonication, the mixture was centrifuged at 10,000 rpm for 5 minutes to obtain a uniformly dispersed SWCNT suspension which was suitable for further processing and integration with perovskite materials.

1.3 Preparation of Perovskite Precursors

The three-step nanotube-perovskite crystallization process begins by combining the SWCNT solution with perovskite precursors. For $MAPbI_3$, 0.17 g of methylammonium iodide (CH_3NH_3I) and 0.46 g of lead iodide (PbI_2) were dissolved in 1 mL DMF and stirred overnight at 60 °C in a controlled atmosphere within a glove box. Similarly, for $CsPbI_3$, 0.25 g of cesium iodide (CsI) and 0.46 g of lead iodide (PbI_2) were dissolved in 1mL DMF and stirred overnight at 100 °C under the same glove box conditions. After stirring, both precursor solutions, prepared at a concentration of 1 M, were filtered through a 0.45 µm pore polytetrafluoroethylene (PTFE) filter to remove undissolved particles, ensuring their suitability for integration with SWCNTs.

1.4 Mixing of Perovskite Precursor with SWCNTs

The prepared perovskite precursor solution (50 µL) was mixed with the SWCNT dispersion (950 µL) via ultrasonication (130 W) for 1 hour. This step was performed to facilitate the uniform distribution of perovskite precursors on the SWCNT surface, ensuring effective interaction between the two materials. Subsequently, 100 µL of the perovskite-SWCNT mixture was

added to 1 mL of ethyl acetate, an anti-solvent, and sonicated for an additional hour. This anti-solvent approach creates a favourable nucleation site for the perovskite to grow around the SWCNTs, forming well-defined nanohybrids.

1.5 Device Fabrication

The resulting mixture was spin-coated onto various substrates, including pre-patterned interdigitated gold electrodes (electrode gap size 3 µm, X&X Technology, UK), glass substrates, and indium tin oxide (ITO) substrates, for subsequent characterization. Spin coating was carried out for 30 seconds at 3000 rpm for homogenous distribution of the mixture on the substrate surface. After deposition, the films substrates were annealed at different temperatures (100 °C for $MAPbI_3$ and 200 °C for $CsPbI_3$ for 30 minutes respectively) to facilitate crystallization and improve the structural integrity of the nanohybrids. The annealing process also helps in optimizing the electronic and optoelectronic properties of the films by enhancing the interaction between the SWCNTs and perovskite nanocrystals.

1.6 Electrical Measurements

Electrical measurements were performed using a probe station (PS-100, Lakeshore) equipped with a semiconducting parameter analyser (Keithley, 4200SCS) at room temperature. The analyser recorded the current through the devices (I_{DS}) where a constant voltage (1 V) was applied to the source and drain electrodes. After the current was stable, lasers of different wavelength typically, 405 nm, 532 nm and 650 nm were shined onto the devices one after the other with a regular interval of time (10 s ON time). We repeated this process to test the reproducibility of the devices. Gate dependence characterization of the devices was carried out by measuring I_{DS} vs V_G curves in the range −10 to 10 V at fixed V_{DS} of 1 V, using HP 4148B Semiconductor Parameter Analyzer.

1.7 Responsivity (R) and Detectivity (D*)

We calculated the responsivity (R) and detectivity (D*) of our devices, being, these two essential parameters employed to evaluate photodetection devices. Responsivity can be obtained by $R=(I_{light}-I_{dark})/(S\times P)$ where I_{light} is the current under illumination, I_{dark} is the current under dark, S is the effective area and P is the power density of light source. The specific detectivity can be calculated by $D^*= RS1/2/(2qI_{dark})1/2$ where R is the responsivity, S is the effective area, and q is the electron charge. The effective area of the device (S) is determined using the formula: S = (Total Area) - (Non-Active Area). Here, the total area refers to the entire region between the device electrodes, while the non-active area represents the portion where no carbon nanotube-perovskite nanohybrids are present between the electrodes.

Conflicts of interest

There are no conflicts to declare.

Acknowledgements

View Article Online
DOI: 10.1039/D6NR00390G

We thank Dr. Suresh Maniarasu, Helmholtz-Zentrum Berlin, Germany for assisting with XPS analysis. We thank Dr. Thibault Degousse and Dr. Teymour Talha-Dean for their valuable inputs. This work was part funded by EP/V010913/1.

References

1. C. Allard, L. Alvarez, J.-L. Bantignies, N. Bendiab, S. Cambré, S. Campidelli, J. A. Fagan, E. Flahaut, B. Flavel, F. Fossard, E. Gaufrès, S. Heeg, J.-S. Lauret, A. Loiseau, J.-B. Marceau, R. Martel, L. Marty, T. Pichler, C. Voisin, ... and W. Wenseleers, *Chemical Society Reviews*, 2024, **53**, 8457–8512.
2. D. Eder, *Chemical Reviews*, 2010, **110**, 1348–1385.
3. R. Xiang, T. Inoue, Y. Zheng, A. Kumamoto, Y. Qian, Y. Sato, M. Liu, D. Tang, D. Gokhale, J. Guo, K. Hisama, S. Yotsumoto, T. Ogamoto, H. Arai, Y. Kobayashi, H. Zhang, B. Hou, A. Anisimov, M. Maruyama, ... and S. Maruyama, *Science*, 2020, **367**, 537–542.
4. M. Shu, Z. Zhang, Z. Dong and J. Xu, *Carbon*, 2021, **182**, 454–462.
5. Q. Ye, X. Xu, A. Paghi, T. Bamford, B. R. Horrocks, A. Houlton, G. Barillaro, S. Dimitrov and M. Palma, *Advanced Functional Materials*, 2021, **31**.
6. N. Roy, M. S. Ahmed, H. K. Lee and S. Jeon, *Nanoscale*, 2024, **16**, 7532–7546.
7. M. Freeley, A. Attanzio, A. Cecconello, G. Amoroso, P. Clement, G. Fernandez, F. Gesuele and M. Palma, *Adv Sci (Weinh)*, 2018, **5**, 1800596.
8. A. Vasylenko, S. Marks, J. M. Wynn, P. V. C. Medeiros, Q. M. Ramasse, A. J. Morris, J. Sloan and D. Quigley, *ACS Nano*, 2018, **12**, 6023–6031.
9. P. Clément, X. Xu, C. T. Stoppiello, G. A. Rance, A. Attanzio, J. N. O'Shea, R. H. Temperton, A. N. Khlobystov, K. R. J. Lovelock, J. M. Seymour, R. M. Fogarty, A. Baker, R. A. Bourne, B. Hall, T. W. Chamberlain and M. Palma, *Angewandte Chemie International Edition*, 2019, **58**, 9928–9932.
10. C. J. Shearer, A. Cherevan and D. Eder, *Advanced Materials*, 2014, **26**, 2295–2318.
11. N. Sultana, H. M. Dewey, A. G. Arellano and J. Budhathoki-Uprety, *Chemistry of Materials*, 2024, **36**, 4034–4053.
12. M. M. Lee, J. Teuscher, T. Miyasaka, T. N. Murakami and H. J. Snaith, *Science*, 2012, **338**, 643–647.
13. H.-S. Kim, C.-R. Lee, J.-H. Im, K.-B. Lee, T. Moehl, A. Marchioro, S.-J. Moon, R. Humphry-Baker, J.-H. Yum, J. E. Moser, M. Grätzel and N.-G. Park, *Scientific Reports*, 2012, **2**.
14. M. A. Green and A. Ho-Baillie, *ACS Energy Letters*, 2017, **2**, 822–830.
15. N.-G. Park, *Materials Today*, 2015, **18**, 65–72.
16. M. Spina, B. Náfrádi, H. M. Tóháti, K. Kamarás, E. Bonvin, R. Gaal, L. Forró and E. Horváth, *Nanoscale*, 2016, **8**, 4888–4893.
17. T. Wu, W. Pisula, M. Y. A. Rashid and P. Gao, *Advanced Electronic Materials*, 2019, **5**, 1900444.
18. Z.-K. Tan, R. S. Moghaddam, M. L. Lai, P. Docampo, R. Higler, F. Deschler, M. Price, A. Sadhanala, L. M. Pazos, D.

Credgington, F. Hanusch, T. Bein, H. J. Snaith and R. H. Friend, *Nature Nanotechnology*, 2014, **9**, 687–692.
19. J. Wang, N. Wang, Y. Jin, J. Si, Z. K. Tan, H. Du, L. Cheng, X. Dai, S. Bai, H. He, Z. Ye, M. L. Lai, R. H. Friend and W. Huang, *Advanced Materials*, 2015, **27**, 2311–2316.
20. Y. Cheng, X. Guo, Y. Shi and L. Pan, *Nanotechnology*, 2024, **35**, 242001.
21. C. Xie, C.-K. Liu, H.-L. Loi and F. Yan, *Advanced Functional Materials*, 2020, **30**, 1903907.
22. J. Zhang, X. G. Hu, K. Ji, S. Zhao, D. Liu, B. Li, P. X. Hou, C. Liu, L. Liu, S. D. Stranks, H. M. Cheng, S. R. P. Silva and W. Zhang, *Nat Commun*, 2024, **15**, 2245.
23. X. Li, F. Cao, D. Yu, J. Chen, Z. Sun, Y. Shen, Y. Zhu, L. Wang, Y. Wei, Y. Wu and H. Zeng, *Small*, 2017, **13**, 1603996.
24. Q. Dong, Y. Fang, Y. Shao, P. Mulligan, J. Qiu, L. Cao and J. Huang, *Science*, 2015, **347**, 967–970.
25. K. X. Steirer, P. Schulz, G. Teeter, V. Stevanovic, M. Yang, K. Zhu and J. J. Berry, *ACS Energy Letters*, 2016, **1**, 360–366.
26. B. Shi, L. Duan, Y. Zhao, J. Luo and X. Zhang, *Advanced Materials*, 2020, **32**, 1806474.
27. G. Vats, B. Hodges, A. J. Ferguson, L. M. Wheeler and J. L. Blackburn, *Adv Mater*, 2023, **35**, e2205459.
28. J. Lee, H. Lee, C. Kim, T. T. T. Nguyen, Y. Kim, G. Jeong, M. Chang, C. Yun and H. Yoon, *J Phys Chem Lett*, 2023, **14**, 8837–8845.
29. Z. Wang, Y. Yu, W. Wang, X. Li, L. Li, X. Wei, W. Zhou, Y. Huang, J. Lin and H. Liu, *ACS Applied Nano Materials*, 2025, DOI: 10.1021/acsanm.5c02337.
30. T. J. Macdonald, M. Batmunkh, C. T. Lin, J. Kim, D. D. Tune, F. Ambroz, X. Li, S. Xu, C. Sol, I. Papakonstantinou, M. A. McLachlan, I. P. Parkin, J. G. Shapter and J. R. Durrant, *Small Methods*, 2019, **3**, 1900164.
31. R. Ihly, A.-M. Dowgiallo, M. Yang, P. Schulz, N. J. Stanton, O. G. Reid, A. J. Ferguson, K. Zhu, J. J. Berry and J. L. Blackburn, *Energy & Environmental Science*, 2016, **9**, 1439–1449.
32. S. Seo, K. Akino, J. S. Nam, A. Shawky, H. S. Lin, H. Nagaya, E. I. Kauppinen, R. Xiang, Y. Matsuo, I. Jeon and S. Maruyama, *Advanced Materials Interfaces*, 2022, **9**, 2101595.
33. P. Schulz, A. M. Dowgiallo, M. Yang, K. Zhu, J. L. Blackburn and J. J. Berry, *J Phys Chem Lett*, 2016, **7**, 418–425.
34. P. Bansal, X. Zhang, H. Wang, P. Kar and W. W. Yu, *Nanoscale Advances*, 2020, **2**, 808–813.
35. Z. Liu, S. Dai, Y. Wang, B. Yang, D. Hao, D. Liu, Y. Zhao, L. Fang, Q. Ou, S. Jin, J. Zhao and J. Huang, *Advanced Functional Materials*, 2019, **30**.
36. Z. Dong, W. Li, H. Wang, X. Jiang, H. Liu, L. Zhu and H. Chen, *Matter*, 2022, **5**, 448–481.
37. Q. B. Zhu, B. Li, D. D. Yang, C. Liu, S. Feng, M. L. Chen, Y. Sun, Y. N. Tian, X. Su, X. M. Wang, S. Qiu, Q. W. Li, X. M. Li, H. B. Zeng, H. M. Cheng and D. M. Sun, *Nat Commun*, 2021, **12**, 1798.
38. I. Ka, L. F. Gerlein, R. Nechache and S. G. Cloutier, *Scientific Reports*, 2017, **7**, 45543.
39. C. Perumal Veeramalai, S. Yang, J. Wei, M. Sulaman, R. Zhi, M. I. Saleem, Y. Tang, Y. Jiang and B. Zou, *ACS Applied Nano Materials*, 2020, **3**, 459–467.
40. A. A. Marunchenko, M. A. Baranov, E. V. Ushakova, D. R. Ryabov, A. P. Pushkarev, D. S. Gets, A. G. Nasibulin and S. V. Makarov, *Advanced Functional Materials*, 2022, **32**, 2109834.
41. H. Zhu, A. Liu, H. L. Luque, H. Sun, D. Ji and Y.-Y. Noh, *ACS Nano*, 2019, **13**, 3971–3981.
42. F. Li, H. Wang, D. Kufer, L. Liang, W. Yu, E. Alarousu, C. Ma, Y. Li, Z. Liu, C. Liu, N. Wei, F. Wang, L. Chen, O. F. Mohammed, A. Fratalocchi, X. Liu, G. Konstantatos and T. Wu, *Advanced Materials*, 2017, **29**, 1602432.
43. J. Hao, Y. H. Kim, S. N. Habisreutinger, S. P. Harvey, E. M. Miller, S. M. Foradori, M. S. Arnold, Z. Song, Y. Yan, J. M. Luther and J. L. Blackburn, *Sci Adv*, 2021, **7**.
44. M. Zhu, H. Yin, J. Cao, L. Xu, P. Lu, Y. Liu, L. Ding, C. Fan, H. Liu, Y. Zhang, Y. Jin, L. M. Peng, C. Jin and Z. Zhang, *Advanced Materials*, 2024, **36**.
45. M. Gao, Y. Park, J. Jin, P.-C. Chen, H. Devyldere, Y. Yang, C. Song, Z. Lin, Q. Zhao, M. Siron, M. C. Scott, D. T. Limmer and P. Yang, *Journal of the American Chemical Society*, 2023, **145**, 4800–4807.
46. M. Song, B. Zhao, B. Li, K. Wang, Y. Jiang, G. Jia, X. Zhao, B. Yu, Y. Li and F. Yang, *Nature Synthesis*, 2025, **4**, 1056–1067.
47. R. J. Kashtiban, C. E. Patrick, Q. Ramasse, R. I. Walton and J. Sloan, *Advanced Materials*, 2023, **35**, 2208575.
48. J. Li, P. Dwivedi, K. S. Kumar, T. Roy, K. E. Crawford and J. Thomas, *Advanced Electronic Materials*, 2020, **7**.
49. G. D. Mildred S. Dresselhaus, Phaedon Avouris, *Carbon Nanotubes: Synthesis, Structure, Properties and Applications*, Springer Berlin, Heidelberg, 1 edn., 2001.
50. B. M. Wieliczka, S. N. Habisreutinger, K. Schutt, J. L. Blackburn and J. M. Luther, *Advanced Energy Materials*, 2023, **13**.
51. M. Kędziora, A. Opala, R. Mastria, L. De Marco, M. Król, K. Łempicka-Mirek, K. Tyszka, M. Ekielski, M. Guziewicz, K. Bogdanowicz, A. Szerling, H. Sigurðsson, T. Czyszanowski, J. Szczytko, M. Matuszewski, D. Sanvitto and B. Piętka, *Nature Materials*, 2024, **23**, 1515–1522.
52. J. Zheng, C. Luo, B. Shabbir, C. Wang, W. Mao, Y. Zhang, Y. Huang, Y. Dong, J. J. Jasieniak, C. Pan and Q. Bao, *Nanoscale*, 2019, **11**, 8020–8026.
53. B. Pradhan, S. Das, J. Li, F. Chowdhury, J. Cherusseri, D. Pandey, D. Dev, A. Krishnaprasad, E. Barrios, A. Towers, A. Gesquiere, L. Tetard, T. Roy and J. Thomas, *Science Advances*, 2020, **6**, eaay5225.
54. W. Xu, Y. Guo, X. Zhang, L. Zheng, T. Zhu, D. Zhao, W. Hu and X. Gong, *Advanced Functional Materials*, 2017, **28**.
55. P. Luo, Y. Zhou, S. Zhou, Y. Lu, C. Xu, W. Xia and L. Sun, *Chemical Engineering Journal*, 2018, **343**, 146–154.
56. Z. Chen, L. Dong, H. Tang, Y. Yu, L. Ye and J. Zang, *CrystEngComm*, 2019, **21**, 1389–1396.
57. *Note: Although XRD samples were prepared in a controlled environment, they often degrade during transfer to the XRD due to the high sensitivity of Cs-based perovskites.*
58. S. M. Bachilo, M. S. Strano, C. Kittrell, R. H. Hauge, R. E. Smalley and R. B. Weisman, *Science*, 2002, **298**, 2361–2366.
59. K. Cui, Y. Qian, I. Jeon, A. Anisimov, Y. Matsuo, E. I. Kauppinen and S. Maruyama, *Advanced Energy Materials*, 2017, **7**, 1700449.
60. I. O. Maciel, N. Anderson, M. A. Pimenta, A. Hartschuh, H. Qian, M. Terrones, H. Terrones, J. Campos-Delgado, A. M. Rao, L. Novotny and A. Jorio, *Nature Materials*, 2008, **7**, 878–883.
61. M. S. Dresselhaus, A. Jorio, M. Hofmann, G. Dresselhaus and R. Saito, *Nano Letters*, 2010, **10**, 751–758.

View Article Online
DOI: 10.1039/D6NR00390G

62. Z. Li, S. A. Kulkarni, P. P. Boix, E. Shi, A. Cao, K. Fu, S. K. Batabyal, J. Zhang, Q. Xiong, L. H. Wong, N. Mathews and S. G. Mhaisalkar, *ACS Nano*, 2014, **8**, 6797–6804.
63. J. Zhang, C. Wang, H. Fu, L. Gong, H. He, Z. Fang, C. Zhou, J. Chen, Z. Chao and J. Fan, *Journal of Alloys and Compounds*, 2021, **862**, 158454.
64. P. Fooladvand, M. Eskandari, D. Fathi and N. Das, *Energy Reports*, 2023, **10**, 3652–3664.
65. T. A. Shastry, P. E. Hartnett, M. R. Wasielewski, T. J. Marks and M. C. Hersam, *ACS Energy Letters*, 2016, **1**, 548–555.
66. L. Du, W. Xiong, W. K. Chan and D. L. Phillips, 2020, **9**, 4689–4701.
67. B. Liu, F. Wu, H. Gui, M. Zheng and C. Zhou, *ACS Nano*, 2017, **11**, 31–53.
68. W. A. Gaviria Rojas and M. C. Hersam, *Advanced Materials*, 2020, **32**, 1905654.
69. S. Ghasemi and K. Moth-Poulsen, *Nanoscale*, 2021, **13**, 659–671.
70. A. D. Franklin, M. C. Hersam and H. S. P. Wong, *Science*, 2022, **378**, 726–732.
71. H. Lu, W. Wu, Z. He, X. Han and C. Pan, *Nanoscale Horizons*, 2023, **8**, 1014–1033.

View Article Online
DOI: 10.1039/D6NR00390G

Data Availability Statement

Additional experimental data can be found in the Supporting Information.